Bulk Scattering Properties for the Remote Sensing of Ice Clouds. Part III: High-Resolution Spectral Models from 100 to 3250 cm^{-1}

BRYAN A. BAUM*

NASA Langley Research Center, Hampton, Virginia

PING YANG AND SHAIMA NASIRI

Texas A&M University, College Station, Texas

ANDREW K. HEIDINGER

NOAA/NESDIS, Silver Spring, Maryland

ANDREW HEYMSFIELD

National Center for Atmospheric Research,+ Boulder, Colorado

JUN LI

Cooperative Institute for Meteorological Satellite Studies, Madison, Wisconsin

(Manuscript received 13 January 2006, in final form 14 June 2006)

ABSTRACT

This study reports on the development of bulk single-scattering models for ice clouds that are appropriate for use in hyperspectral radiative transfer cloud modeling over the spectral range from 100 to 3250 cm^{-1}. The models are developed in a manner similar to that recently reported for the Moderate-Resolution Imaging Spectroradiometer (MODIS); therefore these models result in a consistent set of scattering properties from visible to far-infrared wavelengths. The models incorporate a new database of individual ice-particle scattering properties that includes droxtals, 3D bullet rosettes, hexagonal solid and hollow columns, aggregates, and plates. The database provides single-scattering properties for each habit in 45 size bins ranging from 2 to 9500 μm, and for 49 wavenumbers between 100 and 3250 cm^{-1}, which is further interpolated to 3151 discrete wavenumbers on the basis of a third-order spline interpolation method. Bulk models are developed by integrating various properties over both particle habit and size distributions. Individual bulk models are developed for 18 effective diameters D_{eff}, ranging from $D_{\text{eff}} = 10$ μm to $D_{\text{eff}} = 180$ μm. A total of 1117 particle size distributions are used in the analyses and are taken from analysis of the First International Satellite Cloud Climatology Project Regional Experiment (FIRE)-I, FIRE-II, Atmospheric Radiation Measurement Program intensive operation period (ARM-IOP), Tropical Rainfall Measuring Mission Kwajalein Experiment (TRMM-KWAJEX), and Cirrus Regional Study of Tropical Anvils and Cirrus Layers Florida-Area Cirrus Experiment (CRYSTAL-FACE) data. The models include microphysical and scattering properties such as median mass diameter, effective diameter, single-scattering albedo, asymmetry factor, and scattering phase function. The spectral models are appropriate for applications involving the interpretation of the radiometric measurements of ice clouds acquired by infrared spectrometers such as the Atmospheric Infrared Sounder (AIRS) on the NASA *Aqua* satellite and the Cross-Track Infrared Sounder (CrIS) on the upcoming National Polar-Orbiting Environmental Satellite System (NPOESS) platforms.

* Current affiliation: Space Science and Engineering Center, University of Wisconsin—Madison, Madison, Wisconsin.

+ The National Center for Atmospheric Research is sponsored by the National Science Foundation.

Corresponding author address: Dr. Bryan A. Baum, Space Science and Engineering Center, 1225 W. Dayton St., Madison, WI 53706.
E-mail: bryan.baum@ssec.wisc.edu

DOI: 10.1175/JAM2473.1

1. Introduction

Models of ice-cloud bulk microphysical and single-scattering properties are essential to perform realistic radiative transfer calculations. Such calculations may be used, for example, in remote sensing applications for the inference of optical thickness and effective particle size, in numerical cloud-resolving models, or in general circulation models. The bulk properties include effective diameter D_{eff} or median mass diameter D_m, ice water content (IWC), extinction and scattering efficiencies Q_{ext} and Q_{sca}, respectively, extinction and scattering cross sections σ_{ext} and σ_{sca}, respectively, single-scattering albedo ω, asymmetry parameter g, and the scattering phase function $P(\Theta)$, where Θ is scattering angle. Bulk properties are obtained by integration of individual ice-particle properties over both habit and size distributions.

Ice-cloud bulk single-scattering models assume some knowledge of the particle size and habit distributions as well as the individual particle single-scattering properties for each size and habit. The advent of new techniques for calculating individual particle single-scattering properties combined with a growing set of in situ measurements of ice clouds from various field campaigns provides an opportunity to develop bulk single-scattering models that are derived consistently for a wide range of instruments taking measurements from visible to far-infrared wavelengths.

Baum et al. (2005a,b) incorporated both ice-cloud in situ measurements and recent advances in scattering calculations for a variety of ice-particle habits with the goal of developing narrowband scattering models for use in remote sensing applications. Baum et al. (2005a) focused on the ice-cloud microphysical models, including the ice-particle size and habit distributions. Baum et al. (2005b) discussed the development of a set of narrowband visible and shortwave infrared models for the Moderate-Resolution Imaging Spectroradiometer (MODIS).

Our current work integrates the ice-particle size and habit distributions described by Baum et al. (2005a) with the database of scattering and absorption properties for ice plates, hollow columns, solid columns, 3D bullet rosettes, aggregates, and droxtals described by Yang et al. (2005) and Huang et al. (2004). This integration leads to the creation of a set of bulk single-scattering property models appropriate for use by high-resolution infrared spectrometers in the wavenumber spectrum between 100 and 3150 cm^{-1}, such as the Atmospheric Infrared Sounder (AIRS; Aumann et al. 2003) on the National Aeronautics and Space Administration (NASA) Earth Observing System (EOS) *Aqua* satellite. AIRS is a high-spectral-resolution IR sounder ($\nu/\Delta\nu = 1200$, where ν is the wavenumber and $\Delta\nu$ is the width of a band) with 2378 channels. AIRS measures radiances in the spectral region of 3.74–15.4 μm. The AIRS data are used in conjunction with data from the Advanced Microwave Sounding Unit to provide the vertical profiles of atmospheric temperature and water vapor. However, the data from AIRS are also useful for inferring cloud properties such as cloud effective particle size D_{eff} and optical thickness τ with its high-spectral-resolution IR radiances (Wei et al. 2004; Li et al. 2005; Huang et al. 2004). One-dimensional variational and minimum-residual approaches are used to retrieve the D_{eff} and τ from the AIRS longwave-window- region (790–970 cm^{-1} or 10.31–12.66 μm, and 1050–1130 cm^{-1} or 8.85–9.52 μm) cloudy radiance measurements (Li et al. 2005).

The models discussed herein are built in a way that is consistent with those developed for the MODIS imager (Baum et al. 2005b) that have been implemented for the operational ("collection 5") products. To compare properties inferred from AIRS and MODIS, which are both on the same EOS *Aqua* platform, it is preferable to use consistent bulk single-scattering models in their respective data analyses. In this third part of the series, we extend the method to provide spectral bulk single-scattering models that are appropriate for use with hyperspectral IR data.

Section 2 briefly describes the scattering and absorption property database and the microphysical data collected during various field campaigns. To create bulk single-scattering property models for ice clouds for a given wavenumber, the single-scattering properties for individual ice crystals must be integrated over particle size and habit distributions. Section 3 discusses the method used to integrate various properties over particle size and habit distributions. Results are provided in section 4, and section 5 contains conclusions.

2. Data and models

a. In situ microphysical data

A full description of the in situ data is presented in Baum et al. (2005a) and will be briefly summarized herein. Particle size distributions (PSD) and other microphysical parameters such as median mass diameter D_m) and IWC have been developed for measurements in ice clouds in the midlatitudes, Tropics, and subtropics. These data are derived from the following five field campaigns: 1) the First International Satellite Cloud Climatology Project Regional Experiment (FIRE-I) in Madison, Wisconsin, in 1986; 2) FIRE-II held in Cof-

feyville, Kansas, in 1991; 3) the Atmospheric Radiation Measurement Program (ARM) intensive observation period (IOP) near Lamont, Oklahoma, in the spring of 2000; 4) the Tropical Rainfall Measuring Mission (TRMM) Kwajalein Experiment (KWAJEX) flights near Kwajalein, Marshall Islands, in 1999; and 5) the Cirrus Regional Study of Tropical Anvils and Cirrus Layers Florida-Area Cirrus Experiment (CRYSTAL-FACE) in 2002. Table 1 of Baum et al. (2005a) summarizes the pertinent information regarding the location, altitude, cloud temperature, sampling probes, and the minimum and maximum particle sizes sampled.

From either balloonborne replicators (FIRE-II) or aircraft instrumentation, a set of more than 4000 individual PSDs has been developed. Each PSD is parameterized in the form of a gamma distribution of the form

$$n(D_{\max}) = N_0 D_{\max}^{\mu} e^{-\lambda D_{\max}}, \quad (1)$$

where $D_{\max}$ is the particle maximum dimension and $n(D)$ is the particle concentration per unit volume. On a log–log plot of this equation, N_0 is derived from the intercept, λ is derived from the slope, and μ is derived from the dispersion (Heymsfield et al. 2002). Note that this relationship reduces to an exponential distribution when $\mu = 0$. The values for the intercept, slope, and dispersion were derived for each PSD by matching the three moments (i.e., the first, second, and sixth moments) that provided the best fit over the measured particle size range (Heymsfield et al. 2002). The data are filtered by data from a Rosemount icing probe that detects even minute amounts of liquid water and also cloud temperature to ensure that the particle phase is ice. PSDs are used only from clouds that are colder than −25°C. Of the more than 4000 original PSDs, a total of 1117 PSDs remain after filtering by cloud temperature and the data from the Rosemount icing probe. Heymsfield et al. (2002, 2003, 2004, 2006) and Heymsfield and Miloshevich (2003) provide detailed discussion of the measurement techniques, data descriptions, and analyses and more comprehensive information on N_0, λ, and μ.

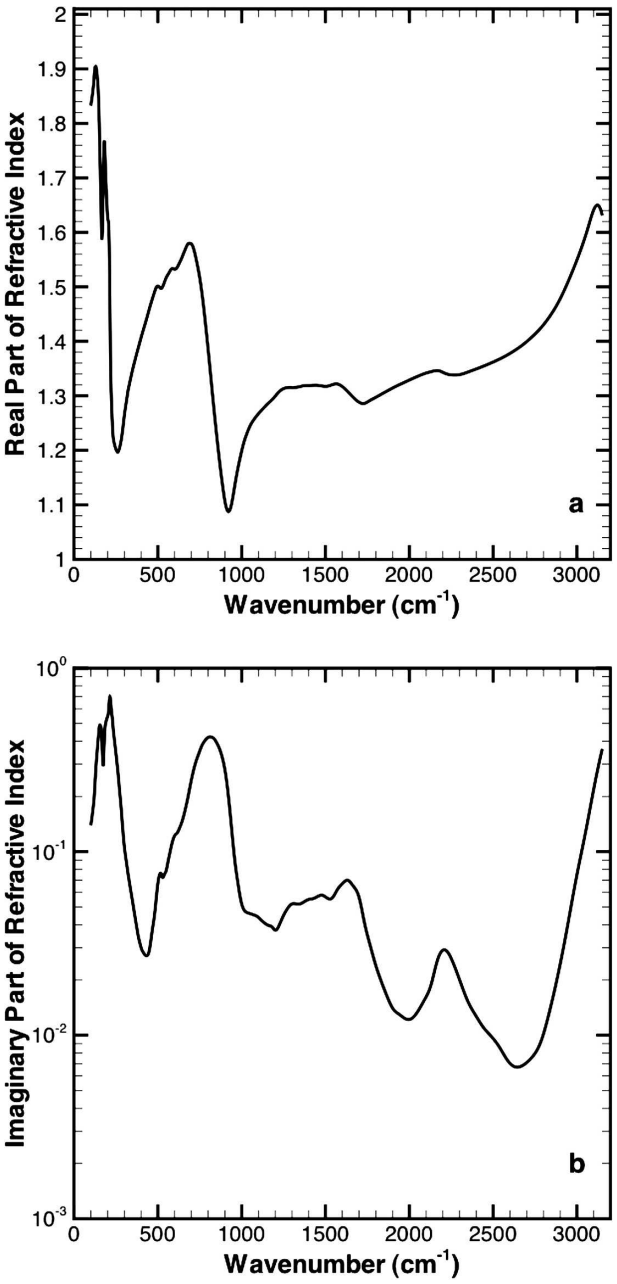

FIG. 1. (a) Real and (b) imaginary parts of the refractive index of ice between 100 and 3250 cm^{-1}, taken from Warren (1984).

b. Ice-particle scattering and absorption properties

For IR radiative transfer calculations, the required single-scattering parameters include extinction and absorption efficiencies, extinction and absorption cross sections (and hence single-scattering albedo), and scattering phase function or asymmetry factor, which is the first-order moment of the phase function. In turn, the scattering and absorption properties of ice particles are determined by the habit (or shape) and size of the particles, the complex refractive index, and the incident wavelength. Figure 1 shows the refractive index for ice in the spectrum between 100 and 3250 cm^{-1} (Warren 1984). Absorption within the ice particles is proportional to the imaginary index of refraction. Strong regions of ice absorption are noted near 200, 800, 1600, 2200, and 3200 cm^{-1}.

Yang et al. (2005) discuss in detail the scattering and absorption properties for a set of ice-particle habits,

with a brief overview provided herein. An extensive database of scattering and absorption properties has been developed for a set of ice particles that include droxtals (spheroidal particles with 20 facets), hexagonal plates, hollow columns, solid columns, three-dimensional bullet rosettes, and aggregates (Yang et al. 2005). The scattering and absorption properties of a particle are determined by the shape and size of the particle, the complex refractive index, and the incident wavelength. The database (Yang et al. 2005) contains properties for 49 wavenumbers between 100 and 3250 cm^{-1} (3 and 100 μm), which are further interpolated to 3151 discrete wavenumbers on the basis of a third-order spline interpolation method. The 49 wavenumbers were chosen to account for the sharp gradients in the refractive index between 100 and 3250 cm^{-1} and to allow interpolation to a higher spectral resolution. For this work, the database has been interpolated to 1 cm^{-1} resolution, which is close to the advanced IR sounder spectral resolution. Therefore, at each wavenumber ν, there is a full set of infrared single-scattering properties for each of the ice crystal habits in 45 size bins spanning a range of 2–9500 μm in terms of particle maximum dimension D. The database contains particle volume $V(\nu, D)$, projected area $A(\nu, D)$, asymmetry factor $g(\nu, D)$, scattering cross section $\sigma_{sca}(\nu, D)$, extinction cross section $\sigma_{ext}(\nu, D)$, and the scattering phase function $P(\Theta, \nu, D)$ at 498 scattering angles Θ from 0° to 180°.

There is no single method that can provide scattering and absorption properties for nonspherical ice particles in the infrared spectral range. In an effort to provide continuous single-scattering properties based on the various numerical methods, Fu et al. (1998) and Yang et al. (2005) discuss in detail the use of a compositing approach; a brief summary is presented here.

The finite-difference time domain (FDTD) method (Yee 1966; Taflove 1995; Yang and Liou 1996a; Sun et al. 1999, 2002) is used when the size parameter is less than 20. The size parameter for an ice particle is defined as $\pi D/\lambda$, where D is the maximum dimension of the particle and λ is the incident wavelength. For size parameters larger than 20, the improved geometric optics method (IGOM; Yang and Liou 1996b) is used. However, a discontinuity exists in the infrared spectrum between the two solutions at size parameters ranging from approximately 20 to 60. Some studies (Fu et al. 1998, 1999; Baran et al. 2003) attribute this discontinuity to a tunneling effect that is neglected in the ray-tracing approach. The composite method seeks to mitigate the problems in the region of discontinuity. After Fu et al. (1998, 1999), the present implementation of the compositing approach combines results from the FDTD method, the IGOM, and Lorenz–Mie theory. The composite method is based on a linear combination of the equivalent-spherical solution and the IGOM results for moderate to large size parameters. The weighting coefficients in the combination are selected to achieve a smooth transition from the FDTD solution to the composite solution. The Lorenz–Mie solutions for spheres with equivalent volumes are applied to hollow columns and plates; the Lorenz–Mie solutions for spheres with equivalent volume-to-projected-area ratios are applied to other habits.

The previous compositing approach is used for extinction efficiency, absorption efficiency, and asymmetry factor for size parameters between 20 and 60. For the scattering phase function, however, the composite method is unnecessary. The relative angular distribution of the scattered energy (i.e., the normalized phase function) computed from IGOM is influenced by the strong absorption within the ice particles in the IR. Because of the strong absorption within the particles, the phase function is basically featureless. The phase functions computed from the IGOM are considered to be approximate solutions for particles having large size parameters (Lee et al. 2003). The scattering phase functions generated by the FDTD and IGOM methods are so similar for the intermediate size parameters (i.e., around 20) that no compositing method is required. For size parameters ≤20, the FDTD-generated phase functions are used; the IGOM-generated phase functions are used for size parameters >20.

3. Bulk microphysical and optical properties

The discussion in this section pertains to the derivation of bulk microphysical and scattering/absorption properties that are obtained by integrating the single-scattering properties for the simulated ice particles (section 2b) over each of the particle size distributions (section 2a) and habit distributions (discussed below in section 3c).

a. Microphysical properties

Based on the ice particles discussed in section 2b, the total projected area and total volume of ice per unit volume of air for a given particle size distribution are given by

$$A_{\mathrm{Tot}} = \sum_{h=1}^{M} \left[\int_{D_{\min}}^{D_{\max}} A_h(D) f_h(D) n(h,D)\, dD \right] \quad \text{and} \tag{2}$$

$$V_{\mathrm{Tot}} = \sum_{h=1}^{M} \left[\int_{D_{\min}}^{D_{\max}} V_h(D) f_h(D) n(h,D)\, dD \right], \tag{3}$$

respectively, where $f_h(D)$ is the ice-particle habit fraction for habit h, $D_{\min}$ and $D_{\max}$ describe the minimum and maximum particle sizes in the distribution, $n(h, D)$ is the number distribution of a specific particle habit h for size D, and $A_h(D)$ and $V_h(D)$ are the area and volume of a specific particle of habit h for size D, respectively. The total mass is obtained by multiplying the total volume by the bulk ice density (0.917 g cm^{-3}).

For satellite retrievals, a common definition for the effective size of any particular PSD is provided by the effective diameter D_{eff}, which is proportional to the ratio of the total volume to the total projected area for a given particle size distribution. After Foot (1988), Francis et al. (1994), and King et al. (2004), D_{eff} is defined as

$$D_{\text{eff}} = \frac{3}{2} \frac{\sum_{h=1}^{M} \left[\int_{D_{\min}}^{D_{\max}} V_h(D) f_h(D) n(h,D)\, dD \right]}{\sum_{h=1}^{M} \left[\int_{D_{\min}}^{D_{\max}} A_h(D) f_h(D) n(h,D)\, dD \right]}. \tag{4}$$

b. Spectral bulk scattering properties

This section provides the derivation of spectral bulk single-scattering properties following the approach discussed in Baum et al. (2005b). The only difference in method is that these single-scattering properties are derived at an individual wavenumber rather than integrated over a spectral response function.

The mean scattering cross section at a specific wavenumber ν is given by

$$\overline{\sigma}_{\text{sca}}(\nu) = \frac{\int_{D_{\min}}^{D_{\max}} \left[\sum_{h=1}^{M} \sigma_{\text{sca},h}(D, \nu) f_h(D) \right] n(D)\, dD}{\int_{D_{\min}}^{D_{\max}} \left[\sum_{h=1}^{M} f_h(D) \right] n(D)\, dD}, \tag{5}$$

where M is the number of habits, D is particle size, and $n(D)$ is the particle density. The habit fraction is defined so that, for each size bin,

$$\sum_{h=1}^{M} f_h(D) = 1. \tag{6}$$

The mean extinction cross section is given by

$$\overline{\sigma}_{\text{ext}}(\nu) = \frac{\int_{D_{\min}}^{D_{\max}} \left[\sum_{h=1}^{M} \sigma_{\text{ext},h}(D, \nu) f_h(D) \right] n(D)\, dD}{\int_{D_{\min}}^{D_{\max}} \left[\sum_{h=1}^{M} f_h(D) \right] n(D)\, dD}. \tag{7}$$

The single-scattering albedo $\overline{\omega}$ is determined by the ratio of the mean scattering and extinction cross sections:

$$\overline{\omega}(\nu) = \frac{\overline{\sigma}_{\text{sca}}(\nu)}{\overline{\sigma}_{\text{ext}}(\nu)}. \tag{8}$$

The scattering phase function $\overline{P}(\Theta)$ is given by

$$\overline{P}(\Theta, \nu) = \frac{\int_{D_{\min}}^{D_{\max}} \left[\sum_{h=1}^{M} P_h(\Theta, D, \nu)\, \sigma_{\text{sca},h}(D, \nu) f_h(D) \right] n(D)\, dD}{\int_{D_{\min}}^{D_{\max}} \left[\sum_{h=1}^{M} \sigma_{\text{sca},h}(D, \nu) f_h(D) \right] n(D)\, dD}, \tag{9}$$

where Θ is the scattering angle.

The asymmetry factor $\overline{g}$ is also weighted by the scattering cross section:

$$\overline{g}(\nu) = \frac{\int_{D_{\min}}^{D_{\max}} \left[\sum_{h=1}^{M} g_h(D, \nu)\, \sigma_{\text{sca},h}(D, \nu) f_h(D) \right] n(D)\, dD}{\int_{D_{\min}}^{D_{\max}} \left[\sum_{h=1}^{M} \sigma_{\text{sca},h}(D, \nu) f_h(D) \right] n(D)\, dD}. \tag{10}$$

c. Particle habit distribution

Baum et al. (2005a) developed the following approach to develop a habit mixture that matched IWC and D_m more closely with the in situ data than did the assumption of a single habit in the PSDs. Although the number of small particles is still uncertain with each PSD, results are shown later that explore the sensitivity of the scattering properties to the number of small particles. Each PSD was divided into four domains based on particle maximum dimension: $D_{\max} \leq 60$ μm, $60 < D_{\max} \leq 1000$ μm, $1000 < D_{\max} \leq 2000$ μm, and $D_{\max} > 2000$ μm. The following restrictions were invoked in developing the habit mixture. Droxtals were used to

represent only the smallest particles, that is, those with D_{max} less than 60 μm. Plates were used for intermediate-sized particles no larger than 1000 μm. Both solid and hollow columns are employed for particles no larger than 2000 μm, based on earlier observations that neither plates nor columns tend to occur at sizes much larger than 1500–2000 μm (Ono 1969; Auer and Veal 1970). Aggregates were used only for particles larger than 1000 μm. Based on these restrictions and size domains, the following distribution was suggested: $D_{max} \leq 60$ μm, 100% droxtals; $60 < D_{max} \leq 1000$ μm, 15% 3D bullet rosettes, 50% solid columns, 35% plates; $1000 < D_{max} \leq 2000$ μm, 45% hollow columns, 45% solid columns, 10% aggregates; and $D_{max} > 2000$ μm, 97% 3D bullet rosettes, 3% aggregates. As noted in Baum et al. (2005a), this habit distribution is one of many that could be derived to minimize differences between the in situ and derived median mass diameter and ice water content values for the set of PSDs.

4. Results

In this section we present the bulk scattering properties obtained from a set of 1117 particle size distributions discussed in detail in Baum et al. (2005a). Results are presented as functions of both the effective diameter and wavenumber.

Figure 2 shows the values for $\bar{g}$ and $\bar{\omega}$ at $\nu = 943$ and 560 cm^{-1}. At 943 cm^{-1}, particle absorption is very strong; however, particle absorption is weak at 560 cm^{-1}. The individual values for $\bar{\omega}$ (Fig. 2a) and $\bar{g}$ (Fig. 2b) are calculated for each PSD at $\nu = 943$ cm^{-1} and are color coded by field campaign. Figures 2c and 2d show $\bar{\omega}$ and $\bar{g}$, respectively, at $\nu = 560$ cm^{-1}. The D_{eff} values range from 40 to 250 μm. The smallest D_{eff} values correspond to the flight track near Nicaragua from a single day of CRYSTAL-FACE PSDs, which were obtained from the coldest cloud in the dataset and which have some of the narrowest size distributions and lowest IWC values. As a way to gain some sense of the sensitivity of the bulk scattering parameters to small particles, the CRYSTAL-FACE PSDs are modified following Baum et al. (2005b). That is, the particle number densities in the smallest size bins (<20 μm) are multiplied by 100 in the first set of calculations and by 1000 in the second set. This is an arbitrary enhancement of only the smallest particles that is performed solely to gain some insight as to the sensitivity of the bulk single-scattering parameters to small particles. Figure 2 also shows the results of multiplying the smallest particles in the CRYSTAL-FACE PSDs by factors of 100 (color coded in magenta) and 1000 (color coded in orange).

Note that at 943 cm^{-1} $\bar{\omega}$ decreases as D_{eff} decreases (Fig. 2a), whereas the opposite behavior is seen for $\bar{\omega}$ at 560 cm^{-1} (Fig. 2c). If one interprets the single-scattering albedo as the probability that a photon will be scattered within the ice particle given an extinction event (Thomas and Stamnes 1999), then the probability of scattering will be lower for small particles at a highly absorbing wavenumber (943 cm^{-1}) than at a less absorbing wavenumber (560 cm^{-1}).

As shown in both Figs. 2b and 2d, there is a tendency for $\bar{g}$ to decrease with D_{eff}, which is attributed to the influence of small particles (e.g., Garrett et al. 2003). Note that $\bar{g}$ decreases quickly as the number of small particles increases. This is expected because small particles tend to scatter isotropically.

As in Baum et al. (2005b), our next goal is to develop single-scattering properties at each wavenumber for a reduced set of D_{eff} values to simplify their application in radiative transfer modeling. In this case, 18 discrete sets of single-scattering properties are developed for $D_{eff} = 10$–180 μm in increments of 10 μm. We noted previously that the way we chose to obtain the bulk scattering parameters for D_{eff} at sizes of less than ~40 μm was to modify the PSDs by increasing the number of small particles (<20 μm) relative to the number of larger particles. The PSDs that fall within a narrow region around each target D_{eff} values are averaged; the width of the region is chosen such that between 10 and 20 individual PSDs can be averaged for each D_{eff}. For each D_{eff} value, a mean and standard deviation are calculated for each microphysical and single-scattering parameter.

Figure 3 presents five different bulk scattering parameters over the wavenumber range from 100 to 3250 cm^{-1}: extinction cross section (cm^2; Fig. 3a), absorption cross section (cm^2; Fig. 3b), extinction efficiency (Fig. 3c), absorption efficiency (Fig. 3d), and asymmetry factor (Fig. 3e). Results are shown for five D_{eff} models ranging from 20 to 100 μm. It is evident from Fig. 3 that the single-scattering properties are dependent on the D_{eff}, with the sensitivity increasing as D_{eff} decreases. Peaks in the absorption cross section and absorption efficiency are noted in the regions of strong absorption (i.e., higher values in the ice imaginary index of refraction). It is interesting to note the sensitivity of asymmetry factor and single-scattering albedo to small particles for the 20-μm D_{eff} model results that is predominant across the spectrum. Small particles consist solely of droxtals, and the scattering properties of these particles are unique (Yang et al. 2003).

Figure 3 shows the bulk scattering properties over the entire wavenumber range from 100 to 3250 cm^{-1}, but radiative transfer calculations must also account for atmospheric absorption by such constituents as water

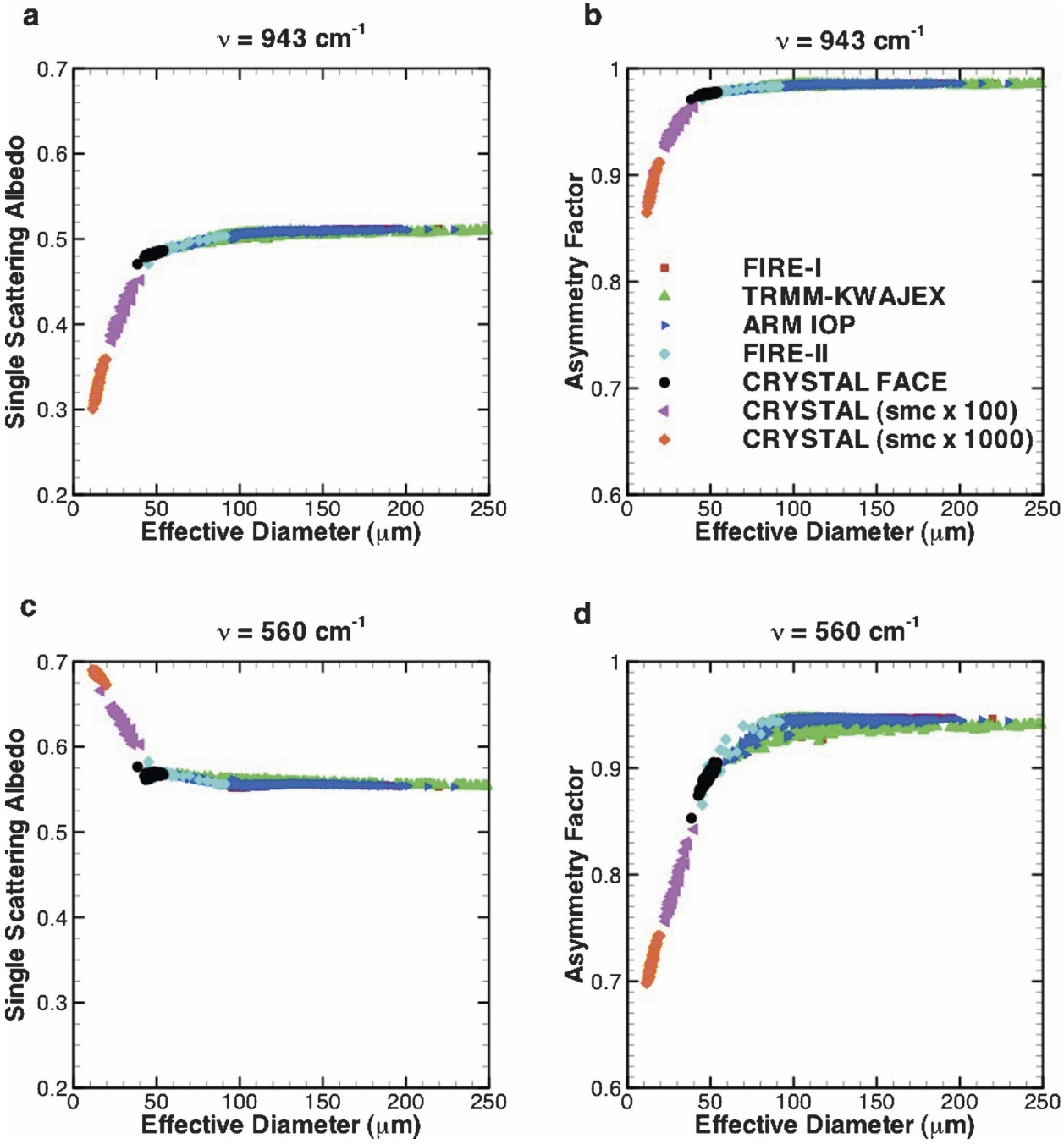

FIG. 2. (left) Single-scattering albedo ϖ and (right) asymmetry factor $\bar{g}$ at wavenumbers of (a), (b) 943 and (c), (d) 560 cm^{-1} calculated from in situ PSDs, assuming a mixture of ice-particle habits. The PSD results are from FIRE-I, FIRE-II, ARM, TRMM-KWAJEX and CRYSTAL-FACE data. Superimposed on the data are the results from a sensitivity study involving the CRYSTAL-FACE PSDs in which the number of particles with sizes less than 20 μm was multiplied by a factor of 100 (magenta symbols) or multiplied by a factor of 1000 (orange symbols).

vapor and ozone. The impact of ice clouds on top-of-atmosphere radiances will be greatest in the window regions of the atmosphere, that is, in regions that are relatively transparent to trace gases, carbon dioxide, ozone, and water vapor. There are several primary window regions between 100 and 3250 cm^{-1}. The spectral region from 400 to 590 cm^{-1} may be thought of as a "dirty" window because it can be moderately transpar-

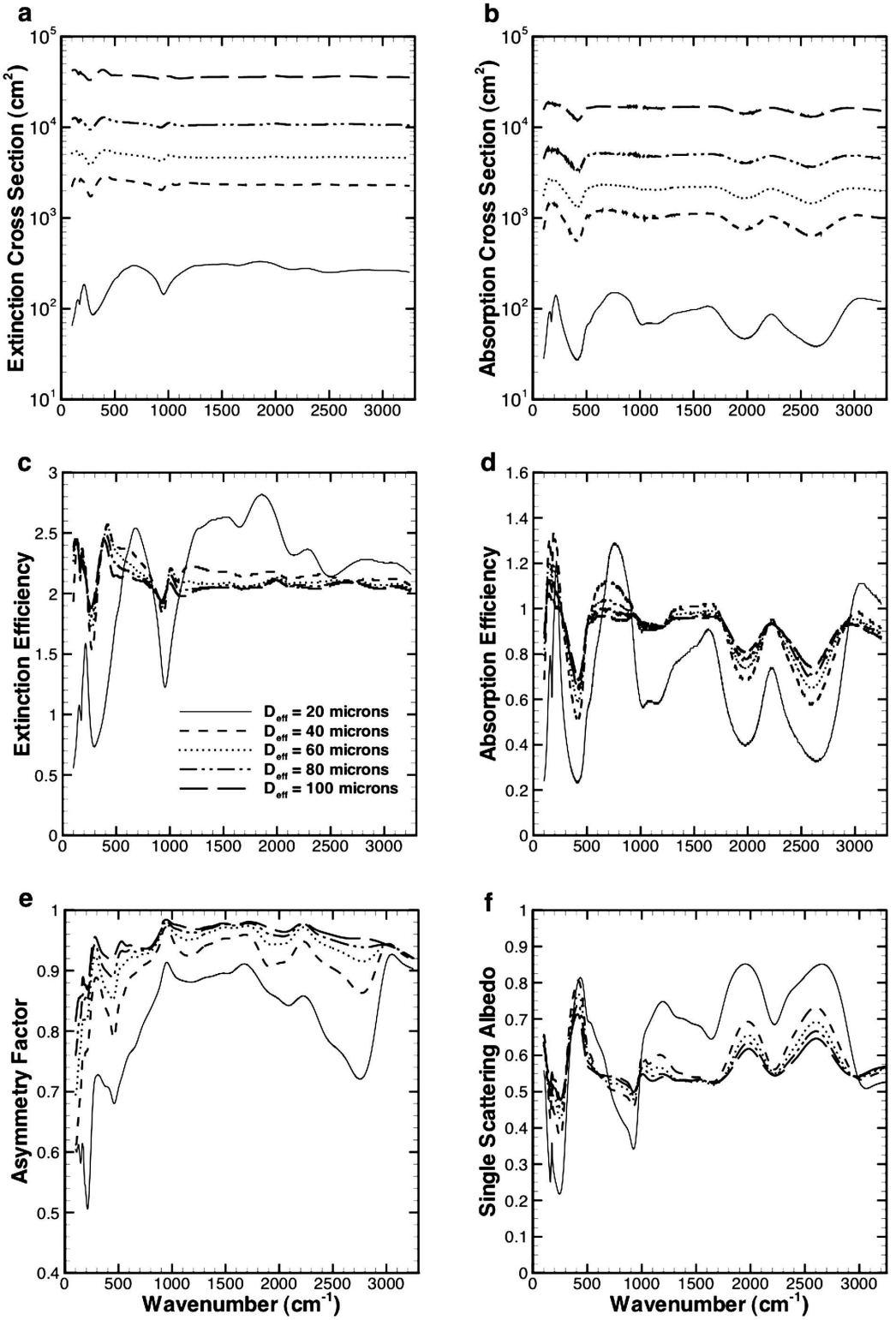

FIG. 3. The variation with wavenumber (between 100 and 3250 cm^{-1}) of (a) extinction cross section (cm^2), (b) absorption cross section (cm^2), (c) extinction efficiency, (d) absorption efficiency, (e) asymmetry factor, and (f) single-scattering albedo for a set of five D_{eff} models ranging from 20 to 100 μm.

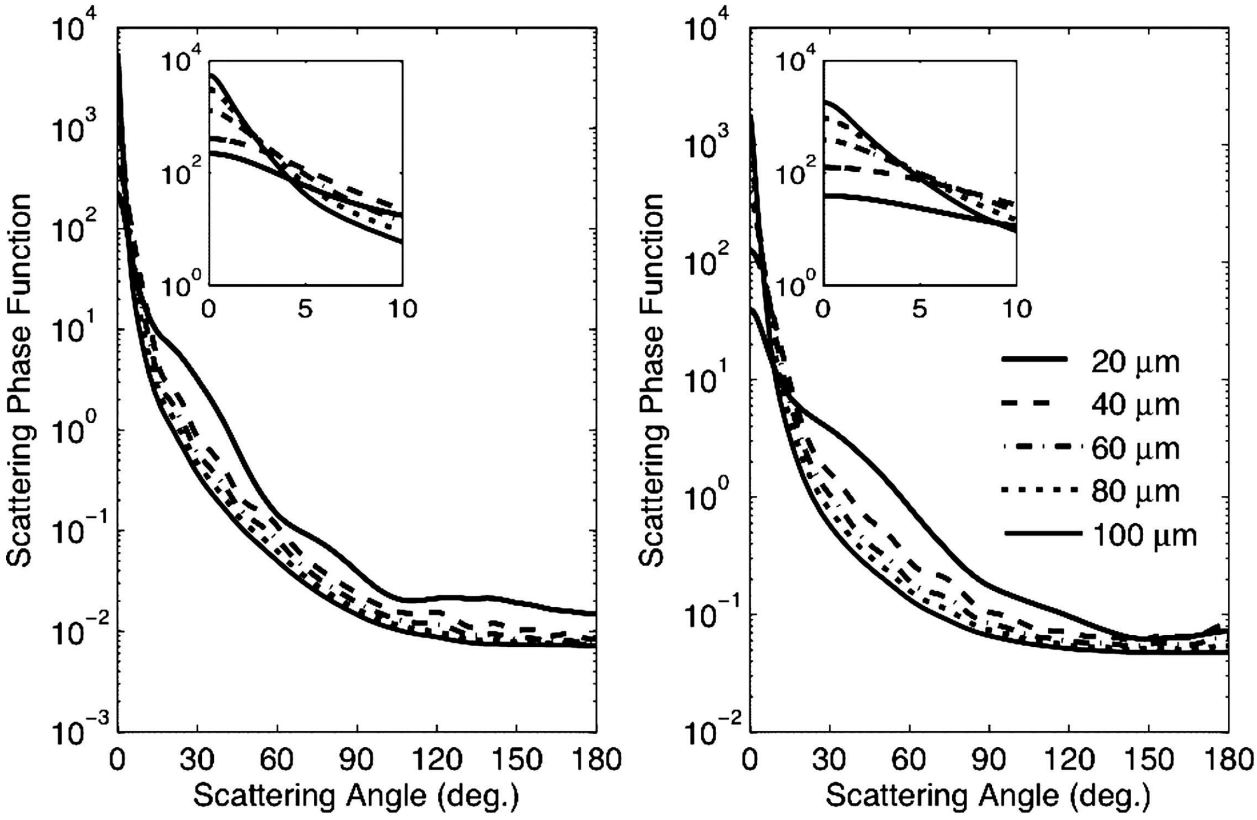

FIG. 4. Scattering phase functions at (left) 943 and (right) 560 cm^{-1} for five D_{eff} values. The insets provide the values of the scattering phase function for scattering angles between 0° and 10°.

ent for cold, dry conditions such as may be found in polar regions. Turner et al. (2003) discuss the potential for using data within this window to aid in determination of cloud thermodynamic phase. The classic thermal IR window broadly spans from 833 to 1250 cm^{-1} (i.e., from 8 to 12 μm). The 800–980 cm^{-1} portion of this broad window band encompasses the "split window" region familiar to users of spaceborne imagers that have 11- and 12-μm bands. The 1100–1250 cm^{-1} region encompasses a less transparent portion of the thermal IR window. Last, the 2400–2900 cm^{-1} window covers a relatively clear spectral range.

In the range from 400 to 590 cm^{-1}, there is some sensitivity of the various single-scattering properties to small particles that are predominant in the 20-μm D_{eff} model. As discussed earlier, this model is derived from artificially increasing the number of particles in the CRYSTAL PSDs for sizes less than 20 μm, that is, in the seven smallest particle size bins. At these small particle sizes, the habit consists solely of droxtals, and these particles have unique single-scattering properties.

The extinction and absorption cross sections in the 800–1200 cm^{-1} spectral region tend to increase monotonically with D_{eff} but display little sensitivity to wavenumber. The extinction efficiency has a value near 2 for the larger D_{eff} values. However, the extinction efficiency displays the most sensitivity to wavenumber for the 20-μm model and reaches a minimum value at approximately 930 cm^{-1}. The asymmetry factor for $D_{eff} >$ 20 μm has values above 0.9 but decreases for the 20-μm model. As particle size becomes much smaller than the wavelength, the scattering tends to become more isotropic. If the scattering is completely isotropic, the asymmetry factor would be zero. The decrease in asymmetry factor with D_{eff} is expected given the greater influence of the smallest particles in the size distribution. The single-scattering albedo tends toward an asymptotic value of 0.5 for the larger D_{eff} values but is generally lower for the 20-μm D_{eff} model.

Figure 4 shows the scattering phase function as a function of D_{eff} at two wavenumbers: 560 and 943 cm^{-1}. Both sets of scattering phase functions are similar in that the magnitude of the forward peaks in the scattering phase functions increases with D_{eff}. This is expected because smaller particles tend to scatter more isotropically. The phase functions are basically smooth except for the case in which droxtals exert a strong influence for the 20-μm D_{eff} model.

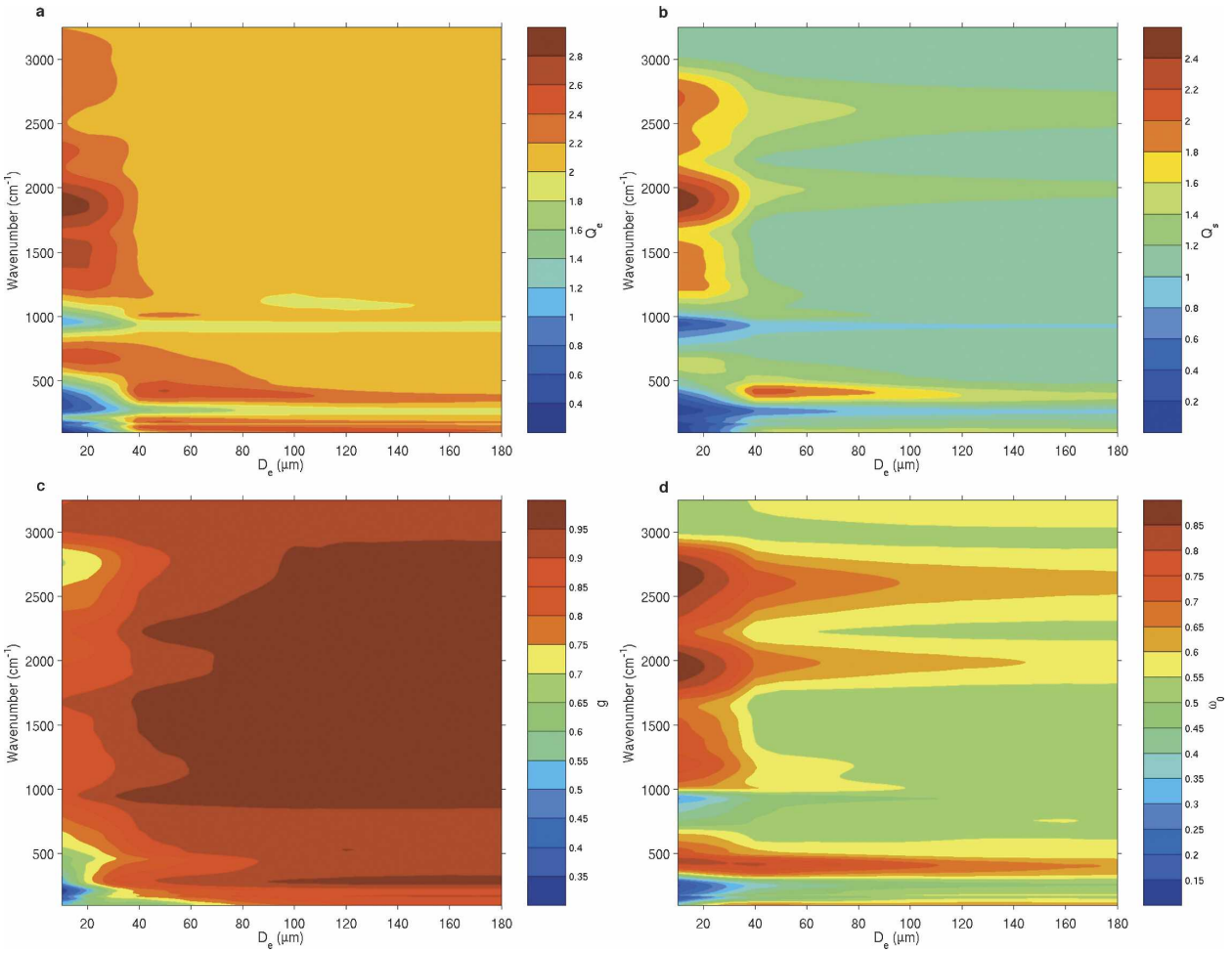

FIG. 5. Contour plots of (a) $\overline{Q}_{\text{ext}}$, (b) $\overline{Q}_{\text{sca}}$, (c) $\overline{g}$, and (d) $\overline{\omega}$ are shown as a function of wavenumber and effective particle size D_{eff}.

The variation of the bulk single-scattering properties with respect to D_{eff} is smooth enough to allow interpolation to a higher D_{eff} resolution. It is possible to interpolate the bulk single-scattering properties to 1-μm resolution in D_{eff}, creating grids with 1-cm^{-1} and 1-μm resolution. In Fig. 5, contour plots of extinction efficiency $\overline{Q}_{\text{ext}}$ (Fig. 5a), scattering efficiency $\overline{Q}_{\text{sca}}$ (Fig. 5b), $\overline{g}$ (Fig. 5c), and $\overline{\omega}$ (Fig. 5d) are shown. For all four properties, the strongest sensitivity to effective size occurs for $D_{\text{eff}} < 50$ μm. There are some interesting observations to make regarding these results. First, note the sharp changes from absorption to scattering regimes, for example, at 1000 and 700 cm^{-1}. Also, $\overline{Q}_{\text{sca}}$ is noted to decrease with increasing D_{eff} across most of the IR region of interest.

5. Summary

This study reports on the development of bulk scattering models for ice clouds that are appropriate for use in hyperspectral radiative transfer simulations at 1-cm^{-1} spectral resolution from 100 to 3250 cm^{-1}. The models incorporate a new database of individual ice-particle scattering properties that includes faceted small particles called droxtals, 3D bullet rosettes, hexagonal solid and hollow columns, aggregates, and hexagonal plates. The database provides scattering properties for each habit in 45 size bins, ranging from 2 to 9500 μm, at a spectral resolution of 1 cm^{-1} that was interpolated from 49 wavelengths for which the light-scattering properties were computed. Bulk models are developed at each wavenumber by integrating each property (e.g., scattering phase function, extinction and absorption cross sections, single-scattering albedo, or asymmetry factor) over both particle habit and size distributions. A set of 1117 PSDs is used in the analyses, each of which was obtained at a cloud temperature lower than −25°C. This set is taken from a larger set of more than 4000 PSDs, which were developed from analysis of FIRE-I, FIRE-II, the ARM (2000) IOP, TRMM-KWAJEX,

and CRYSTAL-FACE data. The ensuing set of models at each wavenumber is simplified into a set of 18 D_{eff} values ranging from 10 to 180 μm to simplify the process of performing radiative transfer simulations. Each D_{eff} model includes microphysical and scattering properties such as median mass diameter, ice water content, single-scatter albedo, asymmetry factor, extinction efficiency, and scattering phase function. The spectral models are appropriate for use by infrared spectrometers such as EOS AIRS and the National Polar-Orbiting Environmental Satellite System (NPOESS) Cross-Track Infrared Sounder (CrIS).

Acknowledgments. This research was sponsored by the Earth Science Enterprise. The authors specifically acknowledge the support and encouragement of Dr. Hal Maring of the NASA Radiation Program at NASA headquarters. Ping Yang also acknowledges support from the National Science Foundation (ATM-0239605) and the NASA Radiation Sciences Program (NNG04GL24G). The views, opinions, and findings contained in this report are those of the authors and should not be construed as an official National Oceanic and Atmospheric Administration or U.S. government position, policy, or decision.

REFERENCES

Auer, A. H., Jr., and D. L. Veal, 1970: The dimension of ice crystals in natural clouds. *J. Atmos. Sci.,* **27,** 919–926.

Aumann, H. H., and Coauthors, 2003: AIRS/AMSU/HSB on the *Aqua* mission: Design, science objectives, data products, and processing systems. *IEEE Trans. Geosci. Remote Sens.,* **41,** 253–264.

Baran, A. J., P. N. Francis, and P. Yang, 2003: A process study of the dependence of ice crystal absorption on particle geometry: Application to aircraft radiometric measurements of cirrus cloud in the terrestrial window region. *J. Atmos. Sci.,* **60,** 417–427.

Baum, B. A., A. J. Heymsfield, P. Yang, and S. M. Thomas, 2005a: Bulk scattering models for the remote sensing of ice clouds. Part I: Microphysical data and models. *J. Appl. Meteor.,* **44,** 1885–1895.

——, P. Yang, A. J. Heymsfield, S. Platnick, M. D. King, Y. X. Hu, and S. M. Thomas, 2005b: Bulk scattering models for the remote sensing of ice clouds. Part II: Narrowband models. *J. Appl. Meteor.,* **44,** 1896–1911.

Foot, J. S., 1988: Some observations of the optical properties of clouds: II Cirrus. *Quart. J. Roy. Meteor. Soc.,* **114,** 145–164.

Francis, P. N., A. Jones, R. W. Saunders, K. P. Shine, A. Slingo, and Z. Sun, 1994: An observational and theoretical study of the radiative properties of cirrus: Some results from ICE'89. *Quart. J. Roy. Meteor. Soc.,* **120,** 809–848.

Fu, Q., P. Yang, and W. B. Sun, 1998: An accurate parameterization of the infrared radiative properties of cirrus clouds for climate models. *J. Climate,* **11,** 2223–2237.

——, W. B. Sun, and P. Yang, 1999: On modeling of scattering and absorption by cirrus nonspherical ice particles at thermal infrared wavelengths. *J. Atmos. Sci.,* **56,** 2937–2947.

Garrett, T. J., H. Gerber, D. G. Baumgardner, C. H. Twohy, and E. M. Weinstock, 2003: Small, highly reflective ice crystals in low-latitude cirrus. *Geophys. Res. Lett.,* **30,** 2132, doi:10.1029/2003GL018153.

Heymsfield, A. J., and L. M. Miloshevich, 2003: Parameterizations for the cross-sectional area and extinction of cirrus and stratiform ice cloud particles. *J. Atmos. Sci.,* **60,** 936–956.

——, A. Bansemer, P. R. Field, S. L. Durden, J. Stith, J. E. Dye, W. Hall, and T. Grainger, 2002: Observations and parameterizations of particle size distributions in deep tropical cirrus and stratiform precipitating clouds: Results from in situ observations in TRMM field campaigns. *J. Atmos. Sci.,* **59,** 3457–3491.

——, S. Matrosov, and B. A. Baum, 2003: Ice water path–optical depth relationships for cirrus and precipitating cloud layers. *J. Appl. Meteor.,* **42,** 1369–1390.

——, A. Bansemer, C. Schmitt, C. Twohy, and M. R. Poellot, 2004: Effective ice particle densities derived from aircraft data. *J. Atmos. Sci.,* **61,** 982–1003.

——, ——, S. L. Durden, R. L. Herman, and T. P. Bui, 2006: Ice microphysics observations in Hurricane Humberto: Comparison with non-hurricane-generated ice cloud layers. *J. Atmos. Sci.,* **63,** 288–308.

Huang, H.-L., P. Yang, H.-L. Wei, B. A. Baum, Y.-X. Hu, P. Antonelli, and S. A. Ackerman, 2004: Retrieval of ice cloud properties from high spectral resolution infrared observations. *IEEE Trans. Geosci. Remote Sens.,* **42,** 842–853.

King, M. D., S. Platnick, P. Yang, G. T. Arnold, M. A. Gray, J. C. Riédi, S. A. Ackerman, and K. N. Liou, 2004: Remote sensing of liquid water and ice cloud optical thickness and effective radius in the Arctic: Application of airborne multispectral MAS data. *J. Atmos. Oceanic Technol.,* **21,** 857–875.

Lee, Y. K., P. Yang, M. I. Mishchenko, B. A. Baum, Y. Hu, H.-L. Huang, W. J. Wiscombe, and A. J. Baran, 2003: On the use of circular cylinders as surrogates for hexagonal pristine ice crystals in scattering calculations at infrared wavelengths. *Appl. Opt.,* **42,** 2653–2664.

Li, J., and Coauthors, 2005: Retrieval of cloud microphysical properties from MODIS and AIRS. *J. Appl. Meteor.,* **44,** 1526–1543.

Ono, A., 1969: The shape and riming properties of ice crystals in natural clouds. *J. Atmos. Sci.,* **26,** 138–147.

Sun, W., Q. Fu, and Z. Chen, 1999: Finite-difference time-domain solution of light scattering by dielectric particles with perfectly matched layer absorbing boundary conditions. *Appl. Opt.,* **38,** 3141–3151.

——, N. G. Loeb, and Q. Fu, 2002: Finite-difference time domain solution of light scattering and absorption by particles in an absorbing medium. *Appl. Opt.,* **41,** 5728–5743.

Taflove, A., 1995: *Computational Electrodynamics: The Finite-Difference Time-Domain Method*. Artech House, 599 pp.

Thomas, G. E., and K. Stamnes, 1999: *Radiative Transfer in the Atmosphere and Ocean*. Cambridge University Press, 517 pp.

Turner, D. D., S. A. Ackerman, and B. A. Baum, 2003: Determination of cloud phase using ground-based observations at 9, 12, and 18 μm. *J. Appl. Meteor.,* **42,** 701–715.

Warren, S. G., 1984: Optical constants of ice from the ultraviolet to the microwave. *Appl. Opt.,* **23,** 1206–1225.

Wei, H., P. Yang, J. Li, B. A. Baum, H. L. Huang, S. Platnick, and

Y. X. Hu, 2004: Retrieval of semitransparent ice cloud optical thickness from Atmospheric Infrared Sounder (AIRS) measurements. *IEEE Trans. Geosci. Remote Sens.,* **42,** 2254–2267.

Yang, P., and K. N. Liou, 1996a: Finite-difference time domain method for light scattering by small ice crystals in three-dimensional space. *J. Opt. Soc. Amer.,* **13A,** 2072–2085.

——, and ——, 1996b: Geometric-optics-integral-equation method for light scattering by nonspherical ice crystals. *Appl. Opt.,* **35,** 6568–6584.

——, B. A. Baum, A. J. Heymsfield, Y. X. Hu, H.-L. Huang, S.-C. Tsay, and S. Ackerman, 2003: Single-scattering properties of droxtals. *J. Quant. Spectrosc. Radiat. Transfer,* **79–80,** 1159–1169.

——, H. Wei, H. L. Huang, B. A. Baum, Y. X. Hu, M. I. Mishchenko, and Q. Fu, 2005: Scattering and absorption property database of various nonspherical ice particles in the infrared and far-infrared spectral region. *Appl. Opt.,* **44,** 5512–5523.

Yee, S. K., 1966: Numerical solution of initial boundary value problems involving Maxwell's equations in isotropic media. *IEEE Trans. Antennas Propag.,* **14,** 302–307.